

# PROPER MOTIONS AND ORIGINS OF SGR 1806–20 AND SGR 1900+14

SHRIHARSH P. TENDULKAR

California Institute of Technology and  
 1200 E California Blvd, MC 249-17, Pasadena, CA 91125, USA

P. BRIAN CAMERON

The Aerospace Corporation and  
 15049 Conference Center Drive, Chantilly, VA 20151-3824, USA

SHRINIVAS R. KULKARNI

California Institute of Technology and  
 1200 E California Blvd, MC 249-17, Pasadena, CA 91125, USA  
*Draft version November 1, 2012*

## ABSTRACT

We present results from high-resolution infrared observations of magnetars SGR 1806–20 and SGR 1900+14 over 5 years using laser-supported adaptive optics at the 10-m Keck Observatory. Our measurements of the proper motions of these magnetars provide robust links between magnetars and their progenitors and provide age estimates for magnetars. At the measured distances of their putative associations, we measure the linear transverse velocity of SGR 1806–20 to be  $350 \pm 100 \text{ km s}^{-1}$  and of SGR 1900+14 to be  $130 \pm 30 \text{ km s}^{-1}$ . The transverse velocity vectors for both magnetars point away from the clusters of massive stars, solidifying their proposed associations. Assuming that the magnetars were born in the clusters, we can estimate the braking index to be  $\sim 1.8$  for SGR 1806–20 and  $\sim 1.2$  for SGR 1900+14. This is significantly lower than the canonical value of  $n = 3$  predicted by the magnetic dipole spin-down suggesting an alternative source of dissipation such as twisted magnetospheres or particle winds.

*Subject headings:* Magnetars: Neutron Stars: SGR 1806–20: SGR 1900+14

## 1. INTRODUCTION

Magnetars were proposed (Thompson & Duncan 1995, 1996) as a unified model to explain the phenomena of soft gamma repeaters (SGRs) and anomalous X-ray pulsars (AXPs). Magnetars, unlike canonical radio pulsars, would have a very high magnetic field strength  $B$  ( $\sim 10^{14} \text{ G}$ ) such that their internal energy was dominated by their magnetic energy rather than their rotational energy. The SGR flares were explained as resulting from violent magnetic reconnections and crustal quakes and the quiescent X-ray emission of AXPs (which is much larger than their spin-down luminosity) was attributed to the decay of intense magnetic fields. The discovery of large period derivatives ( $\dot{P} \sim 10^{-10} \text{ ss}^{-1}$ ; Kouveliotou et al. 1998) confirmed the basic expectation of the magnetar model. For recent reviews of observational and theoretical progress in the field we refer the readers to Mereghetti (2008) and Hurley (2011).

Despite the successes of the magnetar model, we have little understanding of why only some neutron stars are born as magnetars. Originally, Thompson & Duncan (1993) invoked a rapidly spinning ( $\sim$  one to three millisecond) proto-neutron star as essential for strong amplification of a seed magnetic field. The rapidly spinning neutron stars would result in a supernova more energetic than a canonical core-collapse supernova.

The observational support for the formation mechanism of magnetars appears to be lacking. Vink & Kuiper (2006) showed that the three supernova remnants (SNRs) to which three magnetars are best paired, (Kes 73, CTB 109 and N49), are completely consistent with the standard supernova explosion energies.

The offset between SGR 0525–66 (previously known as “5 March 1979”) and its surrounding supernova remnant N49 and the notion that some halo SGRs might explain a fraction of GRBs led to the expectation of SGRs having high space motion (see Rothschild & Lingenfelter 1996). This spawned a number of efforts to measure the space motions of magnetars.

Here, we present astrometric observations of two of the youngest magnetars: SGR 1806–20 and SGR 1900+14. The resulting measurements of proper motion allow us to trace back these two objects to their potential birth sites and additionally measure the space motions as well. The paper is organized as follows. In Section 2, we summarize our knowledge of these two magnetars. In Section 3, we describe our observations, data reduction methodology and analysis techniques for point spread function (PSF) fitting, relative astrometry and photometry. We present the results in Sections 4 and in Section 5 we discuss the significance of our proper motion measurements.

## 2. TARGETS

Table 1 summarizes the essential characteristics of both our targets; SGR 1806–20 and SGR 1900+14. We discuss each target in further detail in the following sec-

TABLE 1  
CHARACTERISTICS OF SGR 1806–20 AND  
SGR 1900+14.

	SGR 1806–20	SGR 1900+14
Period $P$ (sec)	7.6022(7)	5.19987(7)
$\dot{P}$ ( $10^{-11}$ s s $^{-1}$ ) <sup>a</sup>	49	17
$P/\dot{P}$ (kyr)	0.32	1.8
$B_{\text{Surf}}$ ( $10^{14}$ G)	24	7.0
R.A (J2000)	18 <sup>h</sup> 08 <sup>m</sup> 39.337 <sup>s</sup>	19 <sup>h</sup> 07 <sup>m</sup> 14.31 <sup>s</sup>
Dec (J2000)	20° 24′ 39.85″	9° 19′ 19.74″

NOTE. — Refer to <http://www.physics.mcgill.ca/~pulsar/magnetar/main.html>. Positions are from *Chandra* X-ray observations.

<sup>a</sup> Average period derivative calculated from X-ray period measurements from literature. See Section 5.2

tions.

### 2.1. SGR 1806–20

SGR 1806–20 (previously known as GB790107) was identified as a repeating gamma-ray burst with a soft spectrum by Laros et al. (1986). SGR 1806–20 is best known for its giant burst of December 27, 2004 (Hurley et al. 2005; Palmer et al. 2005) which was one of the brightest cosmic flares ever detected. The burst was followed by a long lived radio afterglow (Cameron et al. 2005; Gaensler et al. 2005; Spreeuw et al. 2010) which allowed the precise localization of the source.

#### 2.1.1. Association with Star Cluster

SGR 1806–20 lies in a radio nebula G10.0-0.3 (Kulkarni et al. 1995) which is a part of the W31 HII complex. It was earlier suggested that the massive star LBV 1806–20 and its surrounding radio nebula were associated with SGR 1806–20 (van Kerkwijk et al. 1995) but precise *Chandra* localization (Kaplan et al. 2002) proved that SGR 1806–20 was 14″ away from the center of G10.0-0.3 and 12″ away from LBV 1806–20. A cluster of massive stars, coincident with a mid-IR nebulosity, was discovered by Fuchs et al. (1999) about 7″ to the north of the magnetar.

Table 2 lists all the distance measurements reported to date. We place a higher premium for distance estimates related to the X-ray counterpart of SGR 1806–20 or the associated cluster of massive stars over the estimates to LBV 1806–20, since it is unclear whether LBV 1806–20 is physically near the magnetar. In Table 2, measurements 1–4 are distances to SGR 1806–20 or the cluster of massive stars and measurements 5 and 6 are distances to LBV 1806–20. We adopt a nominal distance of  $9 \pm 2$  kpc which is consistent with all the measurements.

#### 2.1.2. IR Counterpart

Figure 1 shows a  $2 \times 2$  arcsec cutout near SGR 1806–20 from our laser guide star adaptive optics (LGS-AO) supported observations in the  $K_s$  band using the NIRC2 instrument (See Section 3 for details). Star A was suggested as the NIR counterpart for SGR 1806–20 by Kosugi et al. (2005) and independently by Israel et al. (2005) based on NIR variability over the 2004 active

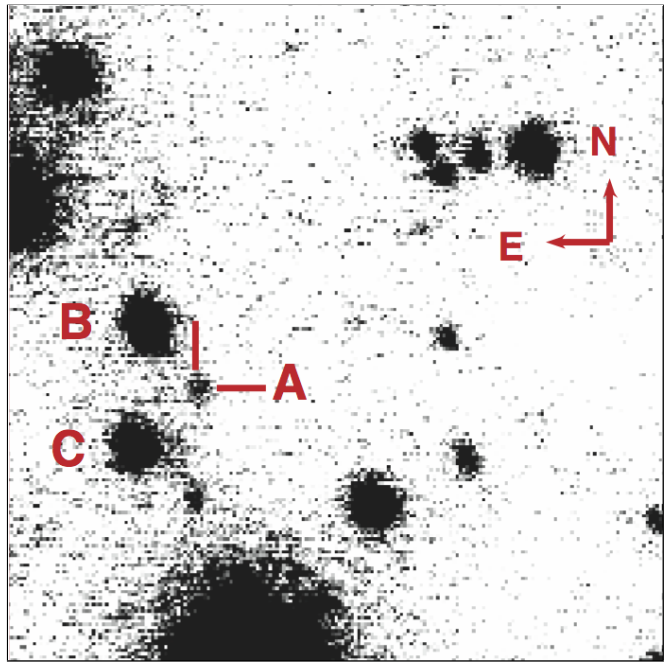


FIG. 1.— A  $2 \times 2$  arcsec cutout near SGR 1806–20 from a  $K_s$  band LGS-AO supported observation from the NIRC2 camera. The IR counterpart, as identified by (Kosugi et al. 2005; Israel et al. 2005) is marked with cross hairs and labeled A as per (Israel et al. 2005) as are stars B and C.

period. Using the NAOS-CONICA instrument on the 8.1-m Very Large Telescope, Israel et al. (2005) monitored SGR 1806–20 on 11 epochs between March and October 2004. They measured a factor of two increase in the flux of the star A with a  $> 9\text{-}\sigma$  confidence. The IR flux increase corresponded well with X-ray flux that also increased by a factor of two in the 2–10 keV and 20–100 keV bands (*XMM-Newton*, *INTEGRAL*; Mereghetti et al. 2005b,a). Our photometric measurements show a factor of three variability in the brightness of the same object (Section 4.1). The identification of the IR counterpart of SGR 1806–20 appears to be secure.

### 2.2. SGR 1900+14

The first bursts from SGR 1900+14 (originally known as B1900+14) were identified by Mazets et al. (1979). A very bright flare was detected on August 27 1998 with a  $\gamma$ -ray peak followed by a 300-s long tail (Hurley et al. 1999; Kouveliotou et al. 1999). Following the burst, a fading radio (Frail et al. 1999) and X-ray source (Hurley et al. 1999) was discovered. These observations led to a precise localization to within  $0.15''$ .

#### 2.2.1. Association with Star Cluster

SGR 1900+14 is located near two objects from which it could have originated. A cluster of massive stars (Vrba et al. 2000), hidden behind two bright M5 super-giants, lies  $12''$  to the east of SGR 1900+14 and a  $10^4$  yr old,  $12'$  diameter SNR G042.8+00.6 lies  $17'$  to the south-east (Mazets et al. 1979; Kouveliotou et al. 1993; Vasisht et al. 1994). If SGR 1900+14 was associated with the cluster of massive stars then it implies a young age and a space velocity close to the canonical value for pulsars. However, if it is associated with the supernova remnant then it would have a very high proper motion.



TABLE 3  
SUMMARY OF OBSERVATIONS OF  
SGR 1806–20.

Date & MJD (UTC MJD)	Filt	Cam	Exp (s)
2005-03-04 53433.641	K <sub>p</sub>	N	1440 ✓
2005-04-30 53490.511	K <sub>p</sub>	N	750
2005-08-10 53592.366	K <sub>p</sub>	W	600
2005-08-11 53593.344	K <sub>p</sub>	W	840
2005-09-26 53639.258	K <sub>p</sub>	N	600 ✓
2006-07-03 53919.403	K <sub>p</sub>	N	2820
2006-08-17 53964.304	K <sub>p</sub>	N	1800 ✓
2007-05-22 54242.487	K <sub>p</sub>	N	1020
2007-06-11 54262.403	K <sub>p</sub>	N	2040
2007-07-16 54297.345	K <sub>p</sub>	N	3000
2007-08-06 54318.329	K <sub>p</sub>	N	2640 ✓
2008-05-21 54607.468	K <sub>p</sub>	N	2460
2008-06-29 54646.407	K <sub>p</sub>	N	3360
2008-07-26 54673.342	K <sub>p</sub>	N	3180 ✓
2010-06-18 55365.442	K <sub>p</sub>	W	80

NOTE. — A ✓ in Column 4 marks the images used for astrometric measurements.

TABLE 4  
SUMMARY OF OBSERVATIONS OF  
SGR 1900+14.

Date & Time (UTC)	Filt	Cam	Exp (s)
2005-04-30 53490.558	K <sub>p</sub>	N	1300 ✓
2005-08-09 53591.434	K <sub>p</sub>	W	2400
2005-08-10 53592.400	K <sub>p</sub>	W	300
2005-09-26 53639.349	K <sub>p</sub>	W	720
2006-07-03 53919.472	K <sub>p</sub>	N	1980
2006-07-04 53920.511	K <sub>p</sub>	N	1920
2006-08-17 53964.439	K <sub>p</sub>	N	1140 ✓
2006-10-13 54021.242	K <sub>p</sub>	N	2220
2007-05-22 54242.550	K <sub>p</sub>	N	1500 ✓
2007-06-11 54262.553	K <sub>p</sub>	N	1260 ✓
2007-06-11 54262.582	H	N	660
2007-08-06 54318.455	K <sub>p</sub>	N	1800 ✓
2007-11-03 54407.229	K <sub>p</sub>	N	1260 ✓
2008-05-21 54607.564	K <sub>p</sub>	N	1260
2008-06-29 54646.471	K <sub>p</sub>	N	3660
2008-07-26 54673.405	K <sub>p</sub>	N	2280 ✓
2008-10-22 54761.227	K <sub>p</sub>	N	1680 ✓
2009-04-06 54927.599	K <sub>p</sub>	N	1620
2009-07-17 55029.340	K <sub>p</sub>	N	2100 ✓
2009-08-04 55047.346	K <sub>p</sub>	N	2100
2009-09-29 55103.226	K <sub>p</sub>	N	2340
2010-06-18 55365.470	K <sub>p</sub>	N	2340 ✓

NOTE. — A ✓ in Column 4 marks the images used for astrometric measurements.

the 10-meter Keck 2 telescope using the Laser Guide Star Adaptive Optics (LGS-AO; Wizinowich et al. 2006; van Dam et al. 2006) and the Near-Infrared Camera 2 (NIRC2). The log of our observations can be found in Tables 3 and 4.

### 3.1.1. NIRC2

The NIRC2 instrument has two modes: wide (W) and narrow (N) with a field-of-view (FoV) of  $\approx 10 \times 10$  arcsecond and  $\approx 40 \times 40$  arcsecond respectively. The corresponding pixel scales are 9.942 milli-arcsecond per pixel and 39.768 milli-arcsecond per pixel. The wide field images were obtained to aid transferring the photometry

and astrometry from the low resolution 2MASS images to the small FoV narrow camera NIRC2 images. The narrow field images were used for the astrometric measurements. Based on weather and faintness of each magnetar, multiple short ( $\sim 20$  s) exposures were chosen to avoid saturating the detector. The typical full width at half maximum (FWHM) achieved in these observations was  $\approx 70$  milli-arcsecond  $\approx 7$  pix.

Each of the NIRC2 narrow camera images was inspected for quality control. Images in which the AO correction was poor were rejected. The shallow images with acceptable AO correction were rejected for astrometry due to the non-detection of the magnetar and/or lack of sufficient reference stars but were used to photometrically calculate upper limits on the brightness. The images used in the final proper motion measurement are denoted by a ✓ in Column 4 of Tables 3 and 4.

### 3.2. Data Analysis

The images from the NIRC2 camera were reduced using the FITS analysis package **pyraf** in a standard manner by subtracting corresponding dark frames and flat-fielded using appropriate dome-flats. A sky fringe frame was made by combining dithered images of multiple targets with the bright stars masked. We used **SExtractor** (Bertin & Arnouts 1996) for the preliminary detection and masking of stars. The fringe frame was subtracted after being scaled to the appropriate sky background level. Before coadding the frames, each frame was corrected for optical distortion using a distortion solution measured for NIRC2<sup>1</sup>.

#### 3.2.1. PSF Fitting

We used the IDL package **StarFinder** (Diolaiti et al. 2000) to perform PSF estimation, fitting and subtraction. This code iteratively estimates a normalized PSF shape from user selected stars, while subtracting faint neighboring stars to minimize the contamination of the PSF estimate. **StarFinder** fits a constant PSF shape over the entire field of view (FoV). This assumption appears to work well for the NIRC2 narrow camera FoV. The uniformity of the PSF over the FoV also mitigates the errors from centroiding variable PSFs.

AO PSFs differ from PSFs obtained from atmospheric seeing limited observations in two aspects: Firstly, because the AO correction decorrelates as a function of distance from the AO reference source (i.e. sodium laser beacon), the PSF varies radially across the field of view. Secondly, since AO correction cannot correct all of the wavefront errors caused by atmospheric turbulence, even on-axis, AO PSFs have a distinctive shape with a sharp diffraction-limited ( $\text{FWHM} \sim \lambda/D_{tel}$ ) core and a wide ( $\text{FWHM} \sim \text{atmospheric seeing}$ ) shallow halo around it. For the Keck AO system, these components are 44 milli-arcsecond and  $\sim 1$  arcsecond respectively. The order of magnitude difference in size and brightness of the two components makes it challenging to accurately measure and subtract the PSF in the image. We describe how both these challenges are handled in the next paragraph.

To further reduce the effect of PSF variations, relative photometry and astrometry measurements were down-

<sup>1</sup> See [http://www2.keck.hawaii.edu/inst/nirc2/forReDoc/post\\_observing/dewarp/](http://www2.keck.hawaii.edu/inst/nirc2/forReDoc/post_observing/dewarp/)

weighted farther away from the object under consideration. The details of the relative weighting are described in Section 3.2.2. The PSF model size was chosen to be 200 pixels (1.95 arcsecond) wide to encompass both the core and the halo of the PSF. The few brightest stars in each of the fields were used for estimating the halo contribution.

### 3.2.2. Relative Astrometry

Cameron et al. (2009) demonstrated a framework for high precision astrometry ( $< 100 \mu\text{arcsecond}$ ) through an optimal estimation technique that availed the correlations in stellar position jitter. We use the same methodology with modifications for including the proper motions of the stars over multiple epochs and an appropriate weighting scheme.

The dominant source of astrometric error in the single epoch, short exposure images of Cameron et al. (2009) was tip-tilt anisoplanatism. For our coadded long exposure images the tip-tilt anisoplanatism is averaged out. We constructed the covariance matrix theoretically using geometry of the field and a typical turbulence profile from Mauna Kea. The residual distortion of the NIRC2 distortion solution has a root-mean-square value of 1 milli-arcsecond. However the distortion residuals have higher values towards the edges<sup>2</sup>. To reduce the effect of residual distortion, especially in images with significant dithering, a separation-weighted measurement scheme (the  $\theta$  term used below) was used to downweight stars far from the target.

To account for the proper motions of all the stars in the field, it was necessary to include the proper motion estimates in the framework and simultaneously estimate a least-squares fit for grid positions and proper motions. Given  $N + 1$  stars detected in the field, the measurement of the offset between the target star and each of the remaining stars results in a set of vectors at each of the  $E$  epochs.

The differential offsets between star 0 and the grid of  $N$  reference stars at epoch  $k$  is written as a single column vector,

$$\mathbf{d}_{0k} = [x_{01}, \dots, x_{0N}, y_{01}, \dots, y_{0N}]_k^T.$$

Here  $x_{ij} = x_j - x_i$  is the distance between the  $x$ -coordinate of the  $j^{\text{th}}$  reference star and the  $x$ -coordinate of the  $i^{\text{th}}$  target star, and likewise for  $y$ . The goal of differential astrometry is to use  $\mathbf{d}$  to determine the position of the target star with respect to the reference grid of stars at each epoch.

We use a linear combination of the elements of  $\mathbf{d}$  with weights  $\mathbf{W}_i$  to obtain the relative position of target star  $i$  at epoch  $k$ ,

$$\mathbf{p}_{ik} = \mathbf{W}_i \mathbf{d}_{ik},$$

where, for example, the weight matrix for star 0,  $\mathbf{W}_0$  is

$$\mathbf{W}_0 = \begin{bmatrix} w_{xx,01} & \dots & w_{xx,0N} & w_{xy,01} & \dots & w_{xy,0N} \\ w_{yx,01} & \dots & w_{yx,0N} & w_{yy,01} & \dots & w_{yy,0N} \end{bmatrix}.$$

We calculated weights as follows:  $w_{xx,ij}^{-1} = w_{yy,ij}^{-1} = \sigma_{ij}^2$ . Here  $\sigma_{ij}^2 = \sigma_m^2 + \sigma_{TJ}^2 \theta_{ij}^2$ , where  $\sigma_{TJ}^2$  is the geometric

mean of the parallel and perpendicular components of the tip-tilt jitter as defined in Equation 1 of Cameron et al. (2009); and  $\theta_{ij}$  is the angular offset between the star  $i$  and the star  $j$ . We have used the notation  $w_{xy,0j}$  to denote the weighting of the offset from the target star ( $i = 0$ ) to star indexed  $j$  in the  $y$  direction which is used to determine the  $x$  component of the target's position,  $\mathbf{p}$ .

We assume a simple linear model for the stellar motion where  $x = z_x + v_x t$ . The differential offsets are thus a column vector,

$$\mathbf{d}_0 = \begin{bmatrix} z_{x,1} + v_{x,1}t - (z_{x,0} + v_{x,0}t) \\ \vdots \\ z_{x,N} + v_{x,N}t - (z_{x,0} + v_{x,0}t) \\ z_{y,1} + v_{y,1}t - (z_{y,0} + v_{y,0}t) \\ \vdots \\ z_{y,N} + v_{y,N}t - (z_{y,0} + v_{y,0}t) \end{bmatrix}$$

and the unknown quantities are,

$$\mathbf{b} = [z_{x,0}, \dots, z_{x,N}, v_{x,0}, \dots, v_{x,N}, \quad (1)$$

$$\dots, z_{y,0}, \dots, z_{y,N}, v_{y,0}, \dots, v_{y,N}]^T. \quad (2)$$

We solve for the variables  $\mathbf{b}$  from the vector  $\mathbf{d}$  given weights  $\mathbf{W}$  in the least squares sense. For a given target, we use the same weights for all epochs. The overall  $x$  and  $y$  shifts of each image (i.e. the registration of the image) are fit as free parameters in this method.

NIRC2 is mounted at the Nasmyth focus of the Keck II telescope. A field-rotator allows the observer to set the position angle of the instrument. Our default position angle was zero degrees (North is up and East is to the left on the detector). However, there are small errors in the setting of the field rotator as well as tracking errors.

To measure this, we chose the images obtained on May 22, 2007 as the reference image for both the targets. The reference images were chosen on the basis of good AO correction and image depth. We computed the rotation-angle and the plate-scale of the image at each epoch with respect to the reference image. We find that the rotation angle is within 0.5 degrees and the image scaling is within 0.1% relative to those of the reference image. The stellar position grids were corrected for the measured rotation and plate-scale changes before measuring their proper motions.

To understand the systematic effects caused by our choice of grid stars, we re-analyzed the centroiding data after randomly eliminating a selected number of stars from the reference grid. We compared the results to those obtained from our entire grid of stars. For example, by eliminating one randomly chosen star out of the 50 stars in the SGR 1900+14 field, the proper motions of all other stars change by  $\Delta(\mu_\alpha, \mu_\delta) = (7.6 \pm 15.4, 17.1 \pm 13.7) \times 10^{-3}$  milli-arcseconds  $\text{yr}^{-1}$ . This is much smaller than our statistical errors of  $\sim 1$  milli-arcsecond  $\text{yr}^{-1}$ . Hence we conclude that the choice of our reference grid is robust and does not add significant errors to our measurements.

### 3.2.3. Galactic Rotation

Since our relative astrometry framework calculates the proper motion of each object with respect to a grid of

<sup>2</sup> [http://www2.keck.hawaii.edu/inst/nirc2/forReDoc/post\\_observing/dewarp/](http://www2.keck.hawaii.edu/inst/nirc2/forReDoc/post_observing/dewarp/)



neighboring stars (i.e. with respect to the average motion of all other stars), it implicitly assumes that the net velocity of the field is zero. However, this is not true since the rotation of the Galaxy and the peculiar velocity of the Sun with respect to the local standard of rest (LSR) cause significant motions at the precision we seek. Our framework cannot measure the net velocity of the field without prior knowledge of the absolute motion of a few stars or equivalently, the absolute non-motion of an extra-galactic object in the field.

To correct for this effect, we need to calculate the mean galactic proper motion of all the stars in the field along the line of sight given by Galactic longitude and latitude ( $l, b$ ). We modelled the differential rotation of the Galaxy and the local velocity of the Sun and calculated the effective proper motion of an object at a given position ( $r, l, b$ ) in the Milky Way, where  $r$  is the distance away from the Sun. We made a model assuming the local velocity of the Sun to be  $(U, V, W) = (10.0, 5.2, 7.2) \text{ km s}^{-1}$  (Dehnen & Binney 1998) and that the Galaxy is rotating with a constant circular speed outside of  $R_1 = 2 \text{ kpc}$  of  $220 \text{ km s}^{-1}$ , decreasing linearly inside of that  $R_1$  (Binney & Tremaine 2008). We set the distance from the Sun to the center of the Galaxy to  $R_0 = 8.0 \text{ kpc}$  (Eisenhauer et al. 2003). From the rotation curve, we calculate the Galactic proper motion  $\vec{\mu}_{\text{Gal}} = [\mu_\alpha, \mu_\delta]_{\text{Gal}}$  of objects at various distances ( $1 \text{ kpc} \leq r \leq 20 \text{ kpc}$ ) in the direction ( $l, b$ ) of the magnetar that are moving with the Galactic flow.

We estimate the number density of stars in the Milky Way using the model calculated by Jurić et al. (2008) using SDSS data. They fit a thin disk, thick disk and a halo to the SDSS data set and calculate the number density function based on their fit. Along the line of sight, the number of stars in our field at a distance  $r$  from the Sun is proportional to  $r^2 \rho(R, Z)$ , where  $\rho(R, Z)$  is the number density of stars at the cylindrical coordinates  $(R(r, l, b), Z(r, l, b))$  in the Milky Way.

For a given field, we calculate the velocity of the field  $\vec{\mu}_{\text{Field}} = [\mu_\alpha, \mu_\delta]_{\text{Field}}$  as the integral of the proper motion weighted with the number density as described above. This gives,

$$\vec{\mu}_{\text{Field}} = \frac{\int_{r_{\min}}^{r_{\max}} r^2 \rho(R(r, l, b), Z(r, l, b)) \times [\mu_{\alpha, \delta}(r, l, b)_{\text{Gal}}] dr}{\int_{r_{\min}}^{r_{\max}} r^2 \rho(R(r, l, b), Z(r, l, b)) dr}.$$

Thus, the total proper motion of each object in the sky is  $\vec{\mu}_{\text{Sky}, i} = \vec{\mu}_{\text{R}, i} + \vec{\mu}_{\text{Field}}$ . Table 5 lists the calculated proper motion for the field and the Galactic proper motion for an object at the distance of the magnetar for both of the targets.

### 3.2.4. Peculiar Motion

We are interested in back-tracing the proper motion of the magnetar to identify its birthsite and estimate the time since it left the birthsite. The relevant motion for this measurement is the relative proper motion between the magnetar and its progenitor. A reasonable assumption is that the progenitor, likely a young massive star, was moving with the Galactic rotation curve. We define the peculiar motion of the magnetar as the difference between its total proper motion  $\vec{\mu}_{\text{Sky}, i}$  and its expected Galactic proper motion  $\vec{\mu}_{\text{Gal}}$ , i.e.  $\vec{\mu}_{\text{Sky}, i} = \vec{\mu}_{\text{Gal}} + \vec{\mu}_{\text{Pec}}$ .

With this definition, the transverse velocity of the magnetar relative to its neighbourhood becomes  $r|\vec{\mu}_{\text{Pec}}|$  in a direction  $\theta$ , s.t.  $\tan(\theta) = (\mu_\alpha/\mu_\delta)_{\text{Pec}}$  East of North.

### 3.2.5. Photometry

**StarFinder** calculates flux estimates for stars in the field by scaling the normalized PSF model to best fit the image. We calculate the photometric zero-point (ZP) for each image by comparing the magnitudes of stars to the 2 Micron All Sky Survey (2MASS) Point Source Catalog (Skrutskie et al. 2006) and to published high-resolution studies of the fields which were anchored to the 2MASS catalog. The details of comparison stars for each field are given in Section 4.

## 4. RESULTS

### 4.1. SGR 1806–20

We performed PSF fitting on the NIRC2 narrow camera images to identify 71 stars through 10 epochs. The positions of these 71 stars were used for relative astrometry.

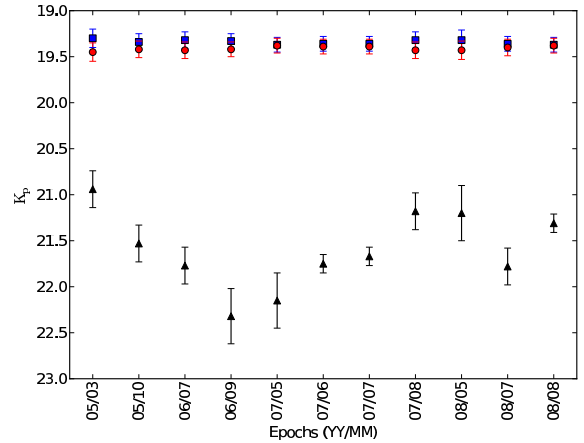


FIG. 3.—  $K_p$  magnitudes of stars around SGR 1806–20 measured over period of 3 years. The circles (red in the online version) correspond to star B and squares (blue in the online version) correspond to star C. The counterpart (star A) of SGR 1806–20 is marked by black triangles. We note a clear variation over a factor of 3 in the brightness of star A.

We performed relative photometry on the stars A, B and C in Figure 1. The photometric zeropoints were measured by matching the magnitudes of stars B and C to the values measured by Kosugi et al. (2005). Figure 3 shows the measured magnitudes of the three stars. We observe a clear factor of 3 variation in the brightness of the IR counterpart of SGR 1806–20, star A, thus securing the identification of the IR counterpart of SGR 1806–20.

#### 4.1.1. Proper Motion

Figure 4 shows the measured proper motions of the stars in the SGR 1806–20 field. The field velocity correction was calculated to be  $(\mu_\alpha, \mu_\delta)_{\text{Field}} = (3.0, 4.8) \text{ milli-arcsecond yr}^{-1}$ . The proper motion of SGR 1806–20 away from a putative progenitor in the galactic flow is  $(\mu_\alpha, \mu_\delta) = (-4.5 \pm 1.4, -6.9 \pm 2.0) \text{ milli-arcsecond yr}^{-1}$ . Assuming a distance of  $9 \pm 2 \text{ kpc}$ , this corresponds to

TABLE 5  
PROPER MOTIONS CALCULATED FROM THE GALACTIC ROTATION MODEL AS DESCRIBED IN  
SECTION 3.2.3.

Object ID	Distance (kpc)	( $l, b$ ) (deg)	$\vec{\mu}_{\text{Field}}$ [ $\mu_\alpha, \mu_\delta$ ] (milli-arcsecond yr $^{-1}$ )	$\vec{\mu}_{\text{Gal}}$ [ $\mu_\alpha, \mu_\delta$ ] (milli-arcsecond yr $^{-1}$ )
SGR 1806–20	$9 \pm 2$	(10.0, –0.2)	[3.0, 4.8]	[ $4.2 \pm 0.9$ , $7.0 \pm 1.8$ ]
SGR 1900+14	$12.5 \pm 1.7$	(43.0, +0.8)	[2.7, 4.6]	[ $2.7 \pm 0.2$ , $4.8 \pm 0.4$ ]

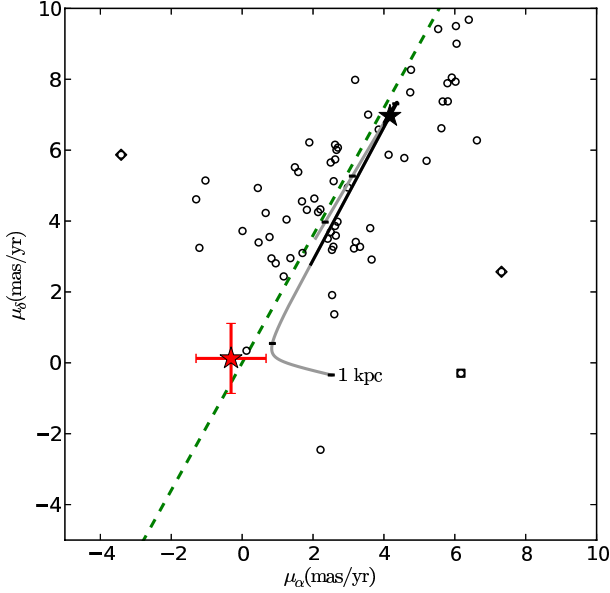


FIG. 4.— The proper motion of 71 stars in the field of reference. SGR 1806–20 is marked by the star with error bars (colored red in the online version). The remaining stars have only their best-fit values (hollow black circles) after adding the bulk motion of the field ( $\vec{\mu}_{\text{Field}} = (3.0, 4.8)$  milli-arcsecond yr $^{-1}$ ) (marked by a black ‘+’). The thick gray line represents the expected motion of stars from 1 to 22.8 kpc along this line of sight, as per the Galactic rotation model presented in Section 3.2.3. Black dashes along the line denote positions 1, 5, 10, 15 and 20 kpc away from the Sun. The section of the line representing objects at a distance of  $9 \pm 2$  kpc from the Sun is marked with a black star and black line to denote the possible motion of the progenitor of SGR 1806–20. The dashed diagonal line (green in the online version) is the locus of objects with  $\mu_b = 0$ , i.e. with zero proper motion along galactic latitude. Other high proper-motion objects, probably halo stars are marked by diamonds. The square marks the nominally high proper-motion object near the edge of the detector. However, this measurement may be corrupted by distortion residuals and hence is not considered any further.

a linear velocity of  $350 \pm 100 \text{ km s}^{-1}$  with an angle of  $213^\circ \pm 10^\circ$  East of North.

Figure 5 shows the direction of motion of SGR 1806–20 with respect to its neighbors. Backtracing this space velocity would put the magnetar close to the cluster of massive stars about 650 years ago.

#### 4.1.2. Other High Proper-Motion Stars

In Figure 4, we mark the high proper-motion objects with diamonds and squares. These stars deviate significantly from the dashed green line marking the locus of objects with  $\mu_b = 0$ , i.e. with zero proper motion along the galactic latitude. These are probably halo stars moving at a high speed through the Galactic disk.

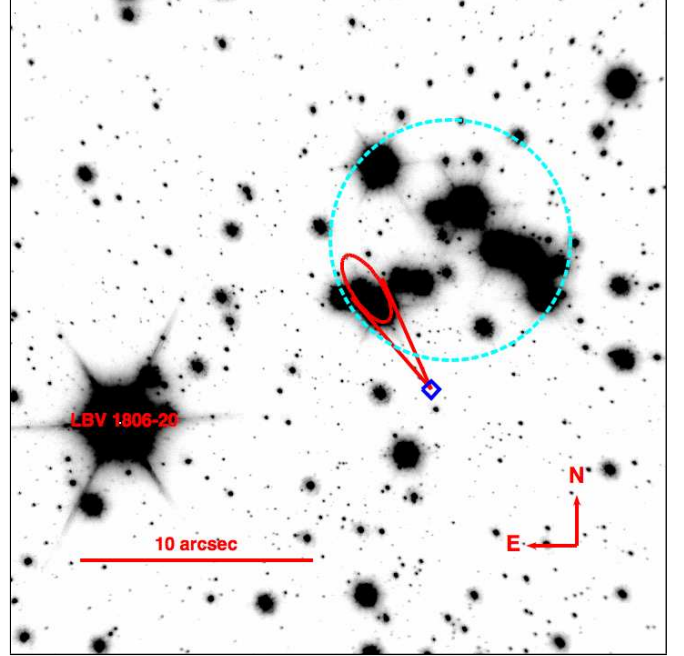


FIG. 5.— The position of SGR 1806–20 (diamond, blue in the online version) traced back by 0.65 kyr is marked by the ellipse (colored red in the online version). The size of the ellipse denotes the positional uncertainty corresponding to the uncertainty in the proper motion measurement. The solid lines (red in the online version) represent the 1- $\sigma$  limits on the angle of motion. The dashed circle (cyan in the online version) denotes the cluster of massive stars corresponding to the mid-IR source of Fuchs et al. (1999). The position of the luminous blue variable LBV 1806–20 is marked.

#### 4.2. SGR 1900+14

We observed SGR 1900+14 at 13 epochs with an exposure time of about 1 hour at each observation. Using  $K_p$ -band photometry and H– $K_p$  band color (at a single epoch), we present variability and color measurements of SGR 1900+14 and its surrounding stars. Our absolute astrometry is matched to positions as reported by Testa et al. (2008) with an accuracy of 6 milli-arcsecond. They reported a 3- $\sigma$  astrometric uncertainty of  $0.81''$  which we adopt for comparison with the radio position for Figure 2.

In three images of the SGR 1900+14 field that had excellent AO correction, we detected a faint source (labelled 10 in Figure 2)  $0.2''$  away from star 3. Source 10 is not detected by Testa et al. (2008) as it was blended with star 3. However, we detected no variation in the combined brightness of star 3 and 10 in our data and the measurements from Testa et al. (2008) within 0.07 mag. Star 10 is a factor of  $\sim 40$  fainter than star 3. With this ratio, assuming no variation in the light from star 3, we

TABLE 6  
PERSISTENT X-RAY LUMINOSITY OF SGR 1900+14 IN  
THE 1-10 keV BAND AS REPORTED BY MEREGHETTI  
ET AL. (2006) AND ISRAEL ET AL. (2008).

Interval (UTC Date)	$F_X$ ( $10^{-12}$ erg cm $^{-2}$ s $^{-1}$ )
20 Sep 2005 - 22 Sep 2005	$4.8 \pm 0.2^a$
25 Mar 2006 - 27 Mar 2006	$4.6 \pm 0.8^b$
28 Mar 2006 - 28 Mar 2006	$6.3 \pm 1.7^b$
01 Apr 2006 - 01 Apr 2006	$5.5 \pm 0.4^a$
08 Apr 2006 - 10 Apr 2006	$5.0 \pm 1.4^b$
11 Apr 2006 - 15 Apr 2006	$5.0 \pm 0.7^b$

<sup>a</sup> Absorbed 0.8-12 keV flux from Mereghetti et al. (2006).

<sup>b</sup> Unabsorbed 1-10 keV flux from Israel et al. (2008).

can constrain the maximum variation in the brightness of star 10 to be 0.4 mag as compared to the 0.48 mag variation measured for star 7 and no variation for star 3 reported by Testa et al. (2008). Thus, we continue to accept star 7 as the IR counterpart of SGR 1900+14.

#### 4.2.1. Variability

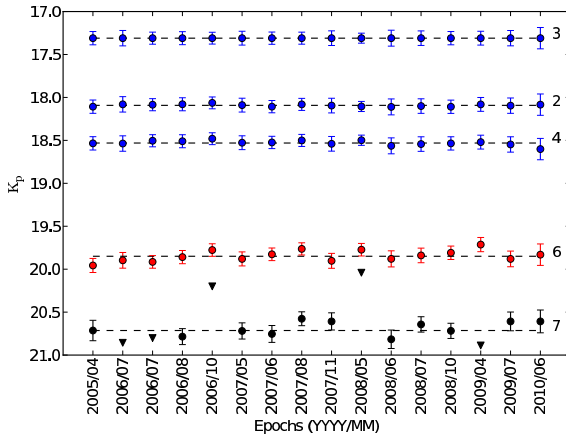


FIG. 6.— Relative photometry light-curves of stars 2-7 (except 5) around SGR 1900+14. To reduce the effect of PSF variations over the field, relative photometry was performed on nearby stars and the absolute calibration was performed by matching stars 2, 3 and 4 to their magnitudes as measured by Testa et al. (2008). The inverted triangles mark 3- $\sigma$  upper limits for star 7 when it was not detected at the edge of star 3.

Figure 6 shows the photometry of stars 2-7 (except 5)<sup>3</sup>. The median magnitude offsets of stars 2, 3 and 4 were used as relative ZP offsets and the absolute ZP offsets were calculated using  $K_p$  magnitudes as reported by Testa et al. (2008). The counterpart suggested by Testa et al. (2008), star 7, was not detected at the edge of star 3 on epochs when the images were not sufficiently deep or the AO performance was not satisfactory. The non-detections were marked with the upper limit on the flux

<sup>3</sup> Star 5 is excepted from all further discussion since it is far away from the X-ray position error circle and does not affect any of the conclusions. Its identification in the middle of the numbering range is an unfortunate quirk of the numbering scheme that was implemented in previous literature.

(black triangles). Including the upper limits on flux, star 7 shows slight variability but it is not conclusive.

During our entire observation period from 2005 to 2010, the X-ray counterpart of SGR 1900+14 showed burst activity in only one period from March to June 2006 (Israel et al. 2008). Unfortunately, we have no IR observations between September 2005 and July 2006. Of these, the AO performance in July 2006 was not satisfactory leading to poor photometry and source confusion. As shown in Table 6, the persistent X-ray luminosity as measured by Israel et al. (2008) and Mereghetti et al. (2006) showed a slight increase in March 2006 and decreased to the pre-burst value by April 2006. Thus the lack of NIR variability is not surprising.

#### 4.2.2. Color Measurement

During the June 11, 2007 observations, we obtained  $K_p$  and H band images of the field. These images were used to determine the colors of stars near SGR 1900+14. No high-resolution H band photometry of this field has been performed previously, so we chose to use 2MASS measurements of bright stars to calculate the ZP offsets for the H band image. The problem with this implementation was that stars bright enough to be included in the 2MASS catalog were saturated in the NIRC2 images which were intended to image the faint magnetar. We rely on the reconstruction of the saturated cores of bright stars by *StarFinder*. This increases the error in photometric measurement and hence in the ZP estimate. We estimate this systematic error in H band ZP to be 0.5 mag. This systematic error changes the scaling on the  $x$ -axis of the color-magnitude diagram (Figure 7) and should not change the conclusion if the magnetar were to have a color distinctly different from other stars in the field.

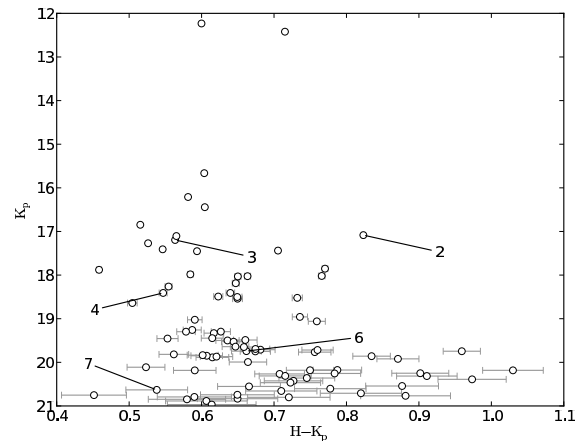


FIG. 7.— H -  $K_p$  color vs  $K_p$  magnitude diagram for 50 stars in the SGR 1900+14 field. Stars 2-7 (except 5) are marked. The H band image zero-point has a systematic uncertainty of  $\sim 0.5$  mag which would effectively only change the scale of the  $x$ -axis.

Figure 7 shows an H -  $K_p$  color vs.  $K_p$  magnitude diagram for the 50 stars in the field. Stars 2-7 are labeled. Neither star 6 nor star 7 have abnormal colors and neither is distinctive. There is no clear structure (for example, a main-sequence) in the color-magnitude



TABLE 7  
H AND  $K_p$  BAND PHOTOMETRY FOR STARS 2–7 (EXCEPT 5) NEAR  
SGR 1900+14. THE ZERO-POINT ERROR IN THE PHOTOMETRY IS 0.5 MAG FOR  
H BAND AND 0.1 MAG FOR  $K_p$  BAND.

Object ID	RA (J2000) (deg)	Dec (J2000) (deg)	H band (mag)	$K_p$ band (mag)
2	19 <sup>h</sup> 07 <sup>d</sup> 14.28 <sup>s</sup>	9° 19′ 18.84″	18.57 ± 0.003	17.98 ± 0.002
3	19 <sup>h</sup> 07 <sup>d</sup> 14.30 <sup>s</sup>	9° 19′ 19.63″	17.76 ± 0.002	17.19 ± 0.001
4	19 <sup>h</sup> 07 <sup>d</sup> 14.28 <sup>s</sup>	9° 19′ 19.78″	18.96 ± 0.005	18.41 ± 0.003
6	19 <sup>h</sup> 07 <sup>d</sup> 14.34 <sup>s</sup>	9° 19′ 19.92″	20.41 ± 0.02	19.74 ± 0.01
7	19 <sup>h</sup> 07 <sup>d</sup> 14.31 <sup>s</sup>	9° 19′ 19.74″	21.17 ± 0.04	20.63 ± 0.02

diagram. This is probably due to the varied distances, ages and extinctions to the stars in this direction. Table 7 lists the H and  $K_p$  band magnitudes of stars 2–7 (except 5) as shown in Figure 7. Magnetars are not known to fall in a specific color band and our lack of understanding of the background physics prevents us from predicting the shape of the IR emission spectrum (Testa et al. 2008). We conclude that the lack of a distinctive color for any star near the location of SGR 1900+14 is not significant.

#### 4.2.3. Proper Motion

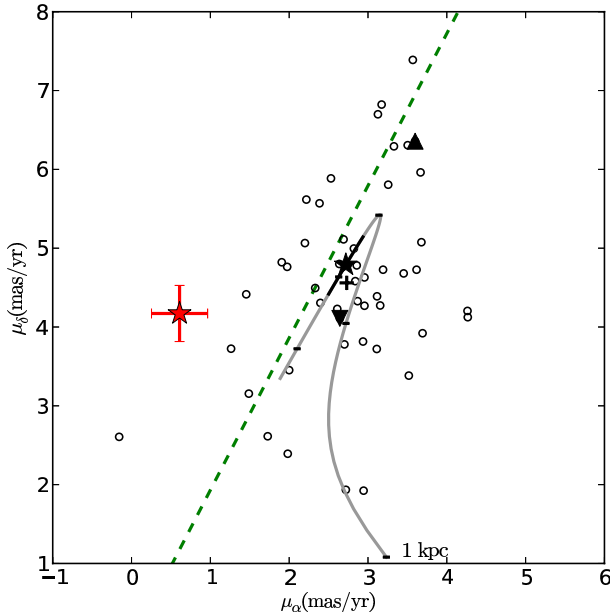


FIG. 8.— The proper motion of 50 stars in the field of SGR 1900+14 in the sky frame of reference. The putative counterpart of SGR 1900+14 is marked by the star with error bars (colored red in the online version). The proper motions of star 6 (solid black triangle) and star 3 (inverted black triangle) seem to lie along the Galactic rotation curve. The remaining stars have only their best-fit values (hollow black circles) after adding the bulk motion of the field ( $\vec{\mu}_{\text{Field}} = (2.7, 4.6)$  milli-arcsecond  $\text{yr}^{-1}$ ) (marked by a black +). The thick gray line represents the expected motion of stars from 1 to 19.8 kpc along this line of sight, as per the Galactic rotation model presented in Section 3.2.3. Black dashes along the line denote positions 1, 5, 10, 15 and 20 kpc away from the Sun. The section of the line representing objects at a distance of  $12.5 \pm 1.7$  kpc from the Sun is marked with a black star and a black line to denote the possible motion of the progenitor of SGR 1900+14. The dashed diagonal line (green in the online version) is the locus of objects with  $\mu_b = 0$ , i.e. with zero proper motion along galactic latitude.

Figure 8 shows the measured proper motions of 50 stars in the neighborhood of SGR 1900+14. The velocity offset, calculated from the galactic rotation, is  $(\mu_\alpha, \mu_\delta)_{\text{Field}} = (2.7, 4.6)$  milli-arcsecond  $\text{yr}^{-1}$ . For star 7, we calculate a proper motion of  $(\mu_\alpha, \mu_\delta) = (-2.1 \pm 0.4, 0.6 \pm 0.5)$  milli-arcsecond  $\text{yr}^{-1}$  away from a putative progenitor moving with the galactic flow. At a distance of  $12.5 \pm 1.7$  kpc, this corresponds to a transverse space velocity of  $130 \pm 30 \text{ km s}^{-1}$ .

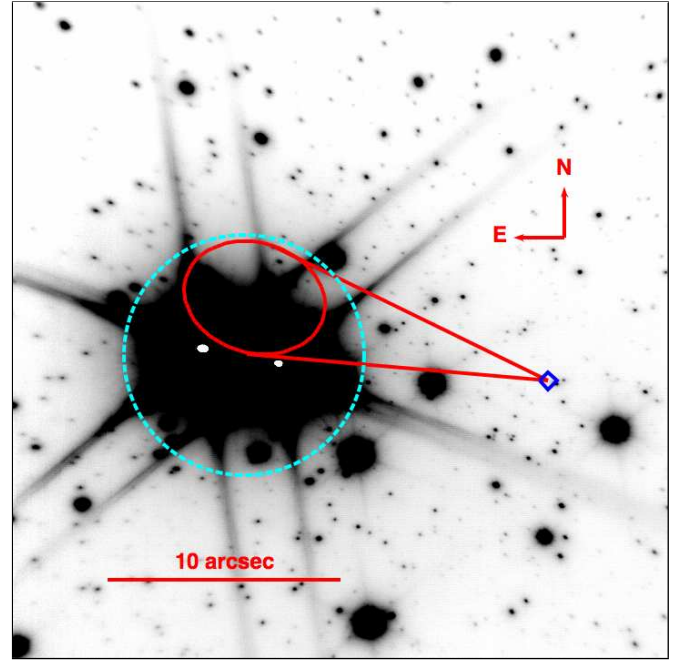


FIG. 9.— The position of the putative counterpart of SGR 1900+14 (blue diamond) traced back by 6 kyr is marked by the solid ellipse (red in the online version). The size of the ellipse denotes the positional uncertainty corresponding to the uncertainty in the proper motion measurement. The solid (red) lines represent the 1- $\sigma$  limits on the angle of motion. The dashed circle (cyan in the online version) denotes the cluster of massive stars (Vrba et al. 2000).

Figure 9 shows the direction of motion of SGR 1900+14 with respect to its neighbors. Backtracing this space velocity would put the magnetar close to the cluster of massive stars about 6 kyr ago.

Star 6 and star 3 are the only two other sources detected inside the 3- $\sigma$  error circle around the radio position of SGR 1900+14. Their velocities are marked by a black triangle (Star 6) and an inverted black trian-

TABLE 8

PROPER MOTIONS MEASURED FOR STARS 2–7 NEAR SGR 1900+14. THE VALUES HAVE BEEN CORRECTED FOR THE GALACTIC ROTATION OFFSETS. THE TRANSVERSE SPACE VELOCITIES ARE CALCULATED ASSUMING A DISTANCE OF 12.5 kpc. 1- $\sigma$  ERROR BARS ON  $\vec{\mu}_{\text{Pec}}$  ARE (0.4, 0.5) MILLI-ARCSECOND YR<sup>-1</sup>.

Object	$\vec{\mu}_{\text{Pec}}$ (milli-arcsecond yr <sup>-1</sup> )	Velocity (km s <sup>-1</sup> )	Direction E of N
2	(-0.11, -0.55)	33 ± 25	191 ± 143
3	(-0.08, -0.67)	40 ± 25	...
4	(-0.74, -2.39)	148 ± 30	197 ± 10
6	(+0.88, +1.58)	107 ± 30	30 ± 12
7	(-2.11, -0.61)	130 ± 30	254 ± 10

gle (Star 3) in Figure 8. Their velocities suggest that these are regular galactic stars moving in the plane of the galaxy (dashed green line).

Table 8 gives the proper motions measured for each of the stars 2–7 along with their corresponding transverse space velocity assuming a distance of 12.5 kpc.

## 5. DISCUSSION

Using LGS adaptive-optics supported near-IR observations, we have measured the proper motions of SGR 1806–20 and SGR 1900+14 to be  $(\mu_\alpha, \mu_\delta) = (-4.5, -6.9) \pm (1.4, 2.0)$  milli-arcsecond yr<sup>-1</sup> and  $(\mu_\alpha, \mu_\delta) = (-2.1, -0.6) \pm (0.4, 0.5)$  milli-arcsecond yr<sup>-1</sup> respectively. These correspond to a linear transverse velocity of  $350 \pm 100$  km s<sup>-1</sup> and  $130 \pm 30$  km s<sup>-1</sup> respectively at the measured distances of their putative associations. Previously, using Very Long Baseline Interferometry (VLBI) at radio wavelengths, transverse linear velocities have been measured only for two magnetars: the AXP 1E 1810–197:  $212 \pm 35$  km s<sup>-1</sup> (Helfand et al. 2007) and the AXP PSR J1550–5418:  $280 \pm 120$  km s<sup>-1</sup> (Deller et al. 2012). The radio counterpart for AXP PSR J1622–4950 has been recently identified by Levin et al. (2010) and would lead to an accurate proper motion measurement with VLBI. With the transverse velocity measurements for two AXPs and two SGRs in the 100 – 400 km s<sup>-1</sup> range, it is highly unlikely that each of these objects has an extremely high radial velocity component. Hence we conclude that magnetars as a family do not possess the high space velocities ( $\sim 1000$  km s<sup>-1</sup>) that were expected earlier (cf. Rothschild & Lingenfelter 1996).

Consider the space velocities of other families of neutron stars in contrast with magnetars. Canonical radio pulsars ( $B \sim 10^{11}$  G) have typical space velocities of  $\sim 200 - 300$  km s<sup>-1</sup> (Hobbs et al. 2005). Tetzlaff et al. (2010) traced the motions of 4 young, hot X-ray bright isolated neutron stars to associate them with progenitors and constrain their ages. They calculated the space velocities of these objects to be  $\sim 350 \pm 180$  km s<sup>-1</sup>. There are a few fast moving pulsars such as PSR J1357–6429, which is a Vela-like radio pulsar has a transverse velocity of  $1600 - 2000$  km s<sup>-1</sup> (Kirichenko et al. 2012), but these seem to be outliers from the family. From these data, we observe that perhaps velocities are not a good discriminator of different groups of neutron stars and their origins.

### 5.1. Association

Our measured proper motions provide very good evidence linking SGR 1806–20 to the cluster of massive stars. The time required for SGR 1806–20 to move from the cluster to its current position is  $650 \pm 300$  yr. It may not be a surprise that one of the younger supernovae in our galaxy resulted from the magnetar. However, SGR 1806–20 lies in the galactic plane behind dust clouds which create very high extinction in the visible wavelengths. Hence, the supernova associated with the magnetar may not have been visible to the naked eye. For SGR 1900+14, we rule out any association with the supernova remnant G 42.8+0.6 and confirm that this magnetar is associated with the star cluster. The time to trace the magnetar back to the cluster is  $6 \pm 1.8$  kyr.

The turn-off masses for the clusters with which the magnetars are associated allow us to place lower limits on the progenitor masses of these magnetars. Currently, progenitor mass estimates exist for three of the magnetars:

SGR 1806–20:  $48^{+20}_{-8} M_\odot$  (Bibby et al. 2008),

CXO J1647–455:  $> 40 M_\odot$  (Muno et al. 2006; Ritchie et al. 2010) and

SGR 1900+14:  $17 \pm 2 M_\odot$  (Davies et al. 2009).

We note that only the two youngest SGRs have a star cluster in their vicinity. The lack of a star cluster in the vicinity of the older SGRs (despite ages of 4 to 10 kyr) suggests that it is not essential that SGRs should be associated with star clusters. Furthermore, the inferred progenitor masses of SGR 1900+14 does not compel us to believe that SGRs arise from massive stars. We conclude that binarity likely has a bigger role in forming SGRs.

### 5.2. Braking Index

If the association of the SGRs with the star clusters is taken for granted, we can constrain the braking index of the magnetars. The braking index  $n$  is calculated from the following implicit equation:

$$n = 1 + \frac{P}{T\dot{P}}(1 - (P_0/P)^{(n-1)}).$$

Here,  $T$  is the kinematic age of the magnetar (time taken to move from cluster to present position) and  $P_0$  is the spin period at birth.

The instantaneous  $\dot{P}$  is known to vary by a factor of three to four corresponding to large variations of braking torque on the magnetar (Woods et al. 2002, 2007). We use the X-ray timing measurements from Kouveliotou et al. (1998); Mereghetti et al. (2005b); Woods et al. (2007); Marsden et al. (1999); Woods et al. (2002, 2003); Mereghetti et al. (2006); Nakagawa et al. (2009) to calculate an average  $\dot{P}$  of  $49 \times 10^{-11}$  s s<sup>-1</sup> for SGR 1806–20 and  $17 \times 10^{-11}$  s s<sup>-1</sup> for SGR 1900+14 from 1996 to 2006.

Assuming  $P_0/P \ll 1$ , we estimate  $n$  to be  $1.76^{+0.65}_{-0.24}$  for SGR 1806–20 and  $1.16^{+0.04}_{-0.07}$  for SGR 1900+14. This is significantly smaller than the canonical value of  $n = 3$  for the magnetic dipole spindown mechanism for pulsars. Low braking indices have been discussed in the context of twisted magnetospheres (eg. Thompson et al. 2002) and particle wind spindown (eg. Tong et al. 2012). However, the large variations in  $\dot{P}$  over tens of years implies that

these measurements cannot be taken at face value.

We would like to thank M. van Kerkwijk and C. Thompson for their critical comments and extensive discussions. The data presented herein were obtained at the W.M. Keck Observatory, which is operated as a scientific

partnership among the California Institute of Technology, the University of California and the National Aeronautics and Space Administration. The Observatory was made possible by the generous financial support of the W.M. Keck Foundation.

Facilities: Keck:II(NIRC2), Keck:II(LGS AO)

## REFERENCES

- Bertin, E., & Arnouts, S. 1996, *A&AS*, 117, 393
- Bibby, J. L., Crowther, P. A., Furness, J. P., & Clark, J. S. 2008, *MNRAS*, 386, L23
- Binney, J., & Tremaine, S. 2008, *Galactic Dynamics: Second Edition* (Princeton University Press)
- Cameron, P. B., Britton, M. C., & Kulkarni, S. R. 2009, *AJ*, 137, 83
- Cameron, P. B., Chandra, P., Ray, A., et al. 2005, *Nature*, 434, 1112
- Davies, B., Figer, D. F., Kudritzki, R.-P., et al. 2009, *ApJ*, 707, 844
- de Luca, A., Caraveo, P. A., Esposito, P., & Hurley, K. 2009, *ApJ*, 692, 158
- Dehnen, W., & Binney, J. J. 1998, *MNRAS*, 298, 387
- Deller, A. T., Camilo, F., Reynolds, J. E., & Halpern, J. P. 2012, *ApJ*, 748, L1
- Diolaiti, E., Bendinelli, O., Bonaccini, D., et al. 2000, in *SPIE Conference Series*, Vol. 4007, SPIE Conference Series, ed. P. L. Wizinowich, 879–888
- Eikenberry, S. S., Matthews, K., LaVine, J. L., et al. 2004, *ApJ*, 616, 506
- Eisenhauer, F., Schödel, R., Genzel, R., et al. 2003, *ApJ*, 597, L121
- Figer, D. F., Najarro, F., & Kudritzki, R. P. 2004, *ApJ*, 610, L109
- Frail, D. A., Kulkarni, S. R., & Bloom, J. S. 1999, *Nature*, 398, 127
- Fuchs, Y., Mirabel, F., Chaty, S., et al. 1999, *A&A*, 350, 891
- Gaensler, B. M., Kouveliotou, C., Gelfand, J. D., et al. 2005, *Nature*, 434, 1104
- Hartmann, D., Vrba, F., Luginbuhl, C., et al. 1996, in *American Institute of Physics Conference Series*, Vol. 366, High Velocity Neutron Stars, ed. R. E. Rothschild & R. E. Lingenfelter, 84–88
- Helfand, D. J., Chatterjee, S., Briskin, W. F., et al. 2007, *ApJ*, 662, 1198
- Hobbs, G., Lorimer, D. R., Lyne, A. G., & Kramer, M. 2005, *MNRAS*, 360, 974
- Hurley, K. 2011, *Physica E Low-Dimensional Systems and Nanostructures*, 43, 681
- Hurley, K., Cline, T., Mazets, E., et al. 1999, *Nature*, 397, 41
- Hurley, K., Boggs, S. E., Smith, D. M., et al. 2005, *Nature*, 434, 1098
- Israel, G., Covino, S., Mignani, R., et al. 2005, *A&A*, 438, L1
- Israel, G. L., Romano, P., Mangano, V., et al. 2008, *ApJ*, 685, 1114
- Jurić, M., Ivezić, Ž., Brooks, A., et al. 2008, *ApJ*, 673, 864
- Kaplan, D. L., Chatterjee, S., Hales, C. A., Gaensler, B. M., & Slane, P. O. 2009, *AJ*, 137, 354
- Kaplan, D. L., Fox, D. W., Kulkarni, S. R., et al. 2002, *ApJ*, 564, 935
- Kirichenko, A., Danilenko, A., Mennickent, R. E., et al. 2012, *ArXiv e-prints*
- Kosugi, G., Ogasawara, R., & Terada, H. 2005, *ApJ*, 623, L125
- Kouveliotou, C., Fishman, G. J., Meegan, C. A., et al. 1993, *Nature*, 362, 728
- Kouveliotou, C., Dieters, S., Strohmayer, T., et al. 1998, *Nature*, 393, 235
- Kouveliotou, C., Strohmayer, T., Hurley, K., et al. 1999, *ApJ*, 510, L115
- Kulkarni, S. R., Matthews, K., Neugebauer, G., et al. 1995, *ApJ*, 440, L61
- Laros, J. G., Fenimore, E. E., Fikani, M. M., Klebesadel, R. W., & Barat, C. 1986, *Nature*, 322, 152
- Levin, L., Bailes, M., Bates, S., et al. 2010, *ApJ*, 721, L33
- Marsden, D., Rothschild, R. E., & Lingenfelter, R. E. 1999, *ApJ*, 520, L107
- Mazets, E. P., Golenetskij, S. V., & Guryan, Y. A. 1979, *Soviet Astronomy Letters*, 5, 343
- McClure-Griffiths, N. M., & Gaensler, B. M. 2005, *ApJ*, 630, L161
- Mereghetti, S. 2008, *A&A Rev.*, 15, 225
- Mereghetti, S., Götz, D., von Kienlin, A., et al. 2005a, *ApJ*, 624, L105
- Mereghetti, S., Tiengo, A., Esposito, P., et al. 2005b, *ApJ*, 628, 938
- Mereghetti, S., Esposito, P., Tiengo, A., et al. 2006, *ApJ*, 653, 1423
- Muno, M. P., Clark, J. S., Crowther, P. A., et al. 2006, *ApJ*, 636, L41
- Nakagawa, Y. E., Mihara, T., Yoshida, A., et al. 2009, *PASJ*, 61, 387
- Palmer, D. M., Barthelmy, S., Gehrels, N., et al. 2005, *Nature*, 434, 1107
- Ritchie, B. W., Clark, J. S., Negueruela, I., & Langer, N. 2010, *A&A*, 520, A48
- Rothschild, R. E., & Lingenfelter, R. E., eds. 1996, *American Institute of Physics Conference Series*, Vol. 366, High Velocity Neutron Stars
- Skrutskie, M. F., Cutri, R. M., Stiening, R., et al. 2006, *AJ*, 131, 1163
- Spreeuw, H., Scheers, B., & Wijers, R. A. M. J. 2010, *A&A*, 509, A99
- Svirski, G., Nakar, E., & Ofek, E. O. 2011, *MNRAS*, 415, 2485
- Testa, V., Rea, N., Mignani, R. P., et al. 2008, *A&A*, 482, 607
- Tetzlaff, N., Neuhäuser, R., Hohle, M. M., & Maciejewski, G. 2010, *MNRAS*, 402, 2369
- Thompson, C., & Duncan, R. C. 1993, *ApJ*, 408, 194
- . 1995, *MNRAS*, 275, 255
- . 1996, *ApJ*, 473, 322
- Thompson, C., Lyutikov, M., & Kulkarni, S. R. 2002, *ApJ*, 574, 332
- Tong, H., Xu, R. X., Song, L. M., & Qiao, G. J. 2012, *ArXiv e-prints*
- van Dam, M. A., Bouchez, A. H., Le Mignant, D., et al. 2006, *PASP*, 118, 310
- van Kerkwijk, M. H., Kulkarni, S. R., Matthews, K., & Neugebauer, G. 1995, *ApJ*, 444, L33
- Vasisht, G., Kulkarni, S. R., Frail, D. A., & Greiner, J. 1994, *ApJ*, 431, L35
- Vink, J., & Kuiper, L. 2006, *MNRAS*, 370, L14
- Vrba, F. J., Henden, A. A., Luginbuhl, C. B., et al. 2000, *ApJ*, 533, L17
- Vrba, F. J., Luginbuhl, C. B., Hurley, K. C., et al. 1996, *ApJ*, 468, 225
- Wachter, S., Ramirez-Ruiz, E., Dwarkadas, V. V., et al. 2008, *Nature*, 453, 626
- Wizinowich, P. L., Le Mignant, D., Bouchez, A. H., et al. 2006, *PASP*, 118, 297
- Woods, P. M., Kouveliotou, C., Finger, M. H., et al. 2007, *ApJ*, 654, 470
- Woods, P. M., Kouveliotou, C., Göğüş, E., et al. 2002, *ApJ*, 576, 381
- . 2003, *ApJ*, 596, 464